Carbon 214 (2023) 118342

Contents lists available at ScienceDirect

Carbon

journal homepage: www.elsevier.com/locate/carbon

Machine learning assisted chemical characterization to investigate the temperature-dependent supercapacitance using Co-rGO electrodes

Xiaoyu Liu [a,1], Dali Ji [a,**,1], Xiaoheng Jin [a], Vanesa Quintano [a,b], Rakesh Joshi [a,*]

[a] School of Materials Science and Engineering, University of New South Wales, Sydney, NSW, 2052, Australia
[b] Catalan Institute of Nanoscience and Nanotechnology (ICN2), CSIC and BIST, Campus UAB, Bellaterra, 08193, Barcelona, Spain

ARTICLE INFO

Keywords:
Graphene oxide
Supercapacitance
Random forest
Machine learning

ABSTRACT

Graphene oxide (GO) intercalated with transition metal oxides (TMOs) has been investigated for optimal supercapacitance performance. However, attaining the best performance requires conducting numerous experiments to find an optimal material composition. This raises an important question; can resource consumption associated with extensive experiments be minimized? Here, we combine the machine learning (ML)-based random forest (RF) model with experimentally observed X-ray photoelectron spectroscopy (XPS) data to construct the complete chemical analysis dataset of Co(III)/Co(II) ratio for thermally synthesized Co-rGO supercapacitor electrodes. The ML predicted dataset could be further coupled with other experiment results, such as cyclic voltammetry (CV), to establish a precise model for predicting capacitance, with ML coefficient of determination (R^2) value of 0.9655 and mean square error value of 6.77. Furthermore, the error between predicted capacitance and experimental validation is found to be less than 8%. Our work indicates that RF can be used to predict XPS data for the TMO-GO system, thereby reducing experimental resource consumption for materials analysis. Moreover, the RF-predicted result can be further utilized in experimental and computational analysis.

1. Introduction

The development of sustainable and renewable energy storage systems has gained significant momentum in recent years, leading to the emergence of non-conventional energy devices such as supercapacitors. Graphene-based supercapacitors have emerged as promising candidates for next-generation energy storage technology because of their high specific area, fast-charging capability, long-life cycle, and low maintenance cost [1–5]. Among these, the combination of graphene oxide (GO) with transition metal oxides (TMOs-GO) has garnered significant attention in recent years [6–9]. Notably, the integration of cobalt oxide (Co oxide) and reduced graphene oxide (rGO) electrodes have demonstrated remarkable potential [10]. The exceptional properties of rGO, including high surface area [11] and facile functionalization [12], coupled with the benefits of Co oxide, such as the introduction of active sites [13,14], improved conductivity [15], and widened voltage window, make this hybrid electrode a highly desirable choice.

Nevertheless, the investigation of these TMOs-GO supercapacitor materials presents significant challenges. Due to various synthesis conditions, materials containing different structures and compositions exceed the scope of exhaustive methods [16,17]. The synergistic interactions among components contribute to the complexity of the system, limiting the ability to predict results intuitively [18,19]. It is technically infeasible to rely solely on experiments to characterize the material and predict the capacitance under all experimental conditions, considering prediction accuracy, time efficiency, and cost-effectiveness [16,17]. Hence, utilizing data-driven methods like machine learning (ML) to accelerate the prediction process is necessary [20]. Multiple ML studies have exhibited that it can predict capacitance, which still relies heavily on the availability of extensive experimental data. It requires collecting experimental conditions and capacitance information from available sources in the literature. However, the data collection method may pose errors in the analysis [16]. Employing ML not only for predicting capacitance but also for assisting material characterization becomes particularly crucial to minimise errors in data analysis.

Recently, ML-assisted material characterization encompasses

* Corresponding author.
** Corresponding author.
E-mail addresses: dali.ji@unsw.edu.au (D. Ji), r.joshi@unsw.edu.au (R. Joshi).
[1] Contributed equally to this work.

https://doi.org/10.1016/j.carbon.2023.118342
Received 5 June 2023; Received in revised form 28 July 2023; Accepted 29 July 2023
Available online 30 July 2023

microscopy enhancement and spectral analysis, with the latter garnering significant attention as an important area of research [21,22]. A common approach in ML-assisted characterization is utilizing existing data and establishing models for predicting or screening new datasets [23]. Recent studies have predominantly focussed on ML-assisted Raman spectroscopy, aiming to predict parameters such as graphene-based materials' thickness, twist angle, and defects [24–26]. Notably, these studies employed an approach that predominantly relies on random forest models (RF) [24–26]. RF can achieve a high level of predictive performance with a relatively low computational burden. Moreover, the RF model is also more suitable for predicting with small datasets. However, there has been limited exploration of utilizing RF models to assist other material's characterizations. This prompts the question of whether these models can be employed in predicting the performance of graphene-based materials, such as capacitance.

In this work, we systematically investigated the relationship among specific capacitance, chemical composition and the synthesis temperature for Co-rGO. We have used a thermal synthesis method for this study [27]. Previously it has been reported that increasing temperature from 150 to 500 °C would increase surface area and enhance conductivity due to a higher C/O ratio in rGO, weakening the capacitance performance [28]. We combined for the first time the machine learning random forest (RF) model with X-ray photoelectron spectroscopy (XPS) data to accurately predict the Co(III)/Co(II) ratio in Co-rGO system synthesized at different temperatures with a remarkable accuracy of 99.9%. Furthermore, based on the RF-assisted XPS results and relevant experimental data, we established RF model to predict the Co-rGO capacitance. The model exhibited a R^2 value of 96.5% and an error (between predicted and experiment data) within 8%. Using these two models, we inferred that the Co(III)/Co(II) ratio of Co in Co-rGO synthesized through thermal methods consistently increased within the temperature range of 200–600 °C. Our work demonstrates that ML, particularly the RF model, can be utilized for predicting XPS results, thereby reducing the consumption of actual XPS measurements. The ML-assisted XPS result predictions can be incorporated into ML models for predictions of materials properties.

2. Materials and methods

2.1. Preparation of GO/Co electrodes

Graphene oxide (purchased from NiSiNa Materials Japan Co., Ltd.) ethanol solution (2 mg/mL) was mixed with $CoCl_2$-ethanol solution (0.1 mg/mL). The $CoCl_2$ amount was appropriately varied in the host GO solution to achieve the compositions 2 wt%, 4 wt%, 6 wt%, 8 wt%, 10 wt %, 12 wt%, 14 wt%, 16 wt% in GO/$CoCl_2$ mixture. An appropriate quantity (i.e., 5 μL) of this mixture (with different mass ratio) was drop casted on carbon fibre paper followed by heating in muffle furnace for duration of 2 h. The samples were named as X-Co-rGO according to heating temperatures (200, 300, 400, 500, 600 °C), where X is the temperature.

2.2. Characterization

2.2.1. RF-assisted XPS data collection

X-ray photoelectron spectroscopy (XPS, Thermo Scientific, UK, ESCALAB250Xi) was used to characterize the valency and ratio of Co (III) to Co(II). It applied 100 eV for survey scans and 20 eV for region scans. In our experiments the C1s = 284.5 eV for graphite act as a reference. We selected a subset of Co-rGO samples for XPS experiments based on different synthesis conditions. These conditions include 200 °C: 2 wt%, 4 wt%, 6 wt%, 8 wt%, 10 wt%, 12 wt%, 14 wt%, 16 wt%; 300 °C: 4 wt%, 8 wt%, 16 wt%; 400 °C: 16 wt%; 500 °C: 16 wt%; 600 °C: 16 wt% (shown in SI 2 Sheet S1).

Based on the above XPS data, we conducted data collection for the RF-assisted XPS model. The input data are the experimental conditions for sample preparation. The output data are corresponding Co(III)/Co (II) ratio obtained from Gaussian fitting of experimentally obtained XPS data. Random forest models (RF) leverage the collective decision-making of multiple individual decision trees to provide accurate predictions and handle complex data patterns [29]. It is regarded as a versatile and powerful ML algorithm due to its high prediction accuracy, robustness to noise as well as the outliers [30,31]. The training and test data of the RF-assisted XPS model were collected from the experimental XPS data of our samples. The training set and test set have a ratio of 80% and 20%, respectively.

2.2.2. RF-assisted XPS model establishment

After data collection, we used Python to perform modelling on the PyCharm software. All screened data were initially accepted impartially without any initial judgment or bias regarding the data validity. The descriptors data were broadly categorized into three categories based on the (1) mass ratio of doping transition oxide, (2) experimental conditions including temperature and corresponding Co(III)/Co(II) ratio.

All the algorithm-specific hyperparameters were tuned via the grid search, which involves splitting the hyperparameter space into user-defined grids, from where the optimal hyperparameter values are searched. The estimators were set as 150. We set max depth and min split as variable values to optimise the results until the results are acceptable. The max depth refers to the maximum depth allowed for decision tree branches in a random forest model. The min split refers to the minimum number of splits allowed during the construction of a decision tree. To enable effective hyperparameter tuning and avoid overfitting simultaneously, the k-fold cross-validation method was used. Considering the dataset size, the K value was set to 10 to prevent overfitting. Further hyperparameter detail set for this study can be found in Supplementary SI 2 Sheet S5.

In this work, two performance functions were applied to analyse the accuracy of output, including R^2 (R squared), MSE (Mean Square Error) and MAE (Mean Absolute Error). The functions are described below [32]:

$$R^2 = 1 - \frac{\sum_i \left(\hat{y}^{(i)} - y^{(i)}\right)^2}{\sum_i \left(\bar{y}^{(i)} - y^{(i)}\right)^2} \tag{1}$$

$$MSE = \frac{1}{m}\sum_i \left(y^{(i)} - \hat{y}^{(i)}\right)^2 \tag{2}$$

$$MAE = \frac{1}{N}\sum_{i=0}^{N} \left|y_i - \hat{y}_i\right| \tag{3}$$

where $\hat{y}^{(i)}$ is the predicted value; $y^{(i)}$ is real value; and $\bar{y}^{(i)}$ indicates the average of real values.

2.2.3. Other material characterization

X-ray diffraction (XRD, PANalytical Empyrean II thin-film) with Co Kα radiation (λ = 0.154 nm) in the range 2θ = 18–30° and 33–64°, with a scan speed of 0.11°/s and step size of 0.05° was used for crystal structure determination. Raman spectroscopy (Renishaw inVia Raman Microscope, 532 nm excitation laser) was also utilized for structural analysis. The surface morphology was studied using scanning electron microscopy (FEI Nova NanoSEM 230 FE-SEM) with energy dispersive X-Ray spectroscopy (EDS) (shown in the supplementary information SI 1).

2.3. Electrochemical measurement

All electrochemical measurements were conducted at ambient temperature on the workstation (WonAtech Electrochemical Workstation ZIVE SP1) with a three-electrode system. The Ag/AgCl electrode work as a reference electrode, and the platinum foil (1 cm × 1 cm) acts as the

counter electrode. The Co-rGO was prepared as a working electrode, and 1.0 M KOH was used as an electrolyte. Cyclic voltammetry (CV) measurements were used to evaluate the electrochemical performance. In our experiments, 100 mV/s scan rate was applied between −1 V and +1V to explore the acceptable potential windows. Based on this, the appropriate potential window (−0.3 to +0.4V) of Co-GO was set and conducted CV analysis with different scan rates (100 mV/s, 200 mV/s, 300 mV/s, 400 mV/s and 500 mV/s). The specific capacitance C (F/g) was calculated with the equation below and electrochemical results [33, 34]:

$$C = \frac{1}{m\nu \times V}\int_{V1}^{V2} IdV \tag{4}$$

Where I is current in Amp; m is the effective electrode mass in g; V is the potential window in V; ν is the scan rate in mV/s; and $\int_{V1}^{V2} IdV$ is the integrated area of the CV curve.

The electrochemical impedance spectroscopy (EIS) was conducted with a potential amplitude of 5 mV in a frequency from 600 kHz to 0.01 Hz. Prior to the EIS measurements, the open circuit potential (OCP) measurements were carried out to stabilize the system, and the obtained OCP value was set as the bias voltage in the EIS measurements.

2.4. RF capacitance model

2.4.1. RF capacitance model data collection

Using the same approach as above, we established a new random forest model RF2 to predict CO-rGO capacitance. The training and testing data of the RF2 capacitance model was collected from RF1 and CV experiments. Similar to RF1, the training set and test set have a ratio of 80% and 20%, respectively. The samples were prepared at different synthesis temperatures which are 200 °C, 300 °C, 400 °C, 500 °C, and 600 °C. For each temperature, the samples with 8 different concentrations: 2 wt%, 4 wt%, 6 wt%, 8 wt%, 10 wt%, 12 wt%, 14 wt%, and 16 wt % were prepared. The CV analysis was performed on each sample with different concentrations at 5 different scanning rates: 100 mV/s, 200 mV/s, 300 mV/s, 400 mV/s, and 500 mV/s to obtain the capacitance data. In total, 200 rows of data were obtained from the experiment (shown in SI 2 Sheet S3). The inputs include synthesis temperatures, mass ratio, scan rate and Co(III)/Co(II) ratios. The output is the corresponding capacitance value for the Co-rGO system.

2.4.2. RF capacitance model establishment

Based on the above data, we established the capacitance model. The descriptors data were broadly categorized into five categories based on the (1) capacitance of samples, (2) mass ratio of doping transition oxide, (3) Co(III)/Co(II) obtained from RF1 and experimental conditions,

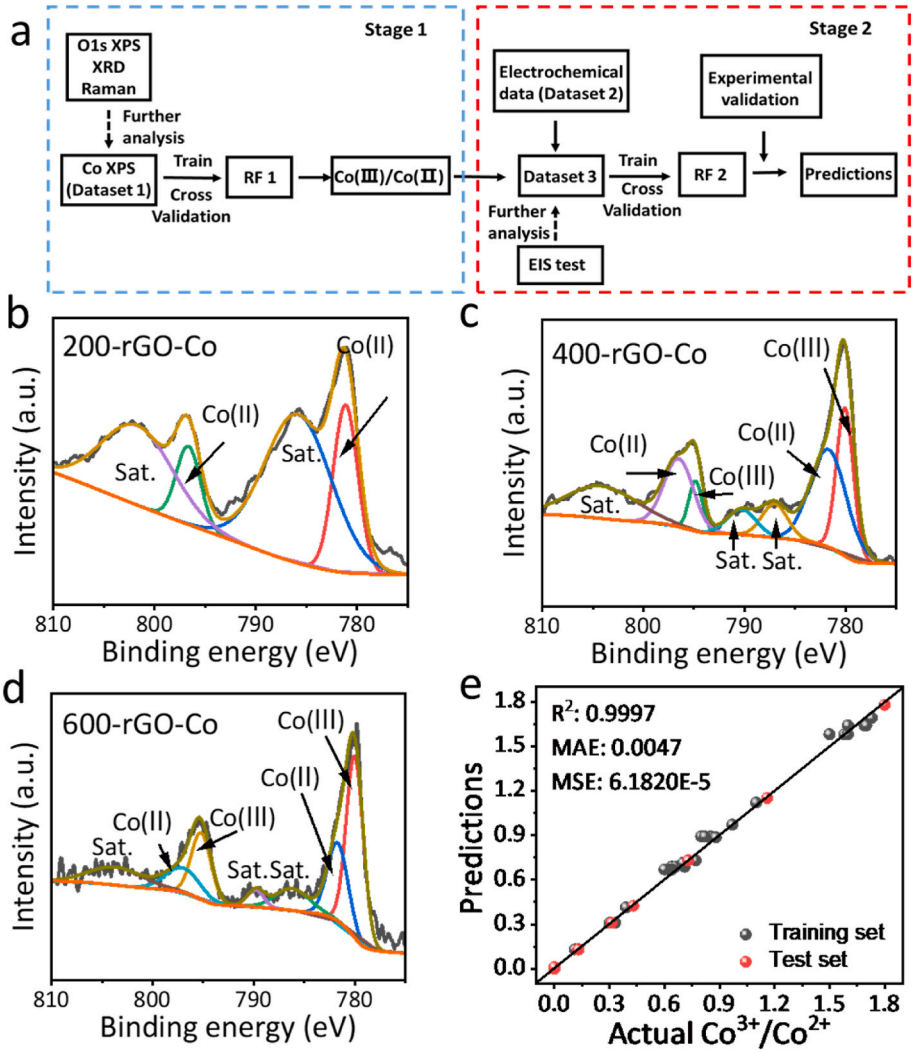

Fig. 1. (a) Workflow of the whole project. (b–d) XPS spectrum of Co 2p form samples prepared at 200, 400, 600 °C. (e) Comparison of actual Co(III)/Co(II) and predicted Co(III)/Co(II). Different colours represent one iteration of the training and testing sets. (A colour version of this figure can be viewed online.)

which include (4) synthesis temperature and (5) scan rate.

Here, the RF model parameters are similar to RF1, with estimators set at 150. No specific values are set for the maximum depth and minimum sample split. Consequently, the 10-fold cross-validation method was utilized to validate model accuracy as RF1. Similarly, the accuracy of the predicting capacitance model is validated through R^2, MSE, and MAE.

3. Results and discussion

Fig. 1 illustrates the two stages of this study. In the first stage, XPS data of samples with 8 different mass ratios at 200 °C, 4 different mass ratios at 300 °C, and with only one mass ratio of 16 wt% at 400 °C, 500 °C, 600 °C was analysed to obtain the Co(III)/Co(II) ratio. These synthesis temperatures and mass ratios were regarded as inputs. The corresponding Co(III)/Co(II) ratio worked as the output to train the first random forest model (RF1). Additionally, we employ other characterization techniques such as XRD, Raman, and SEM to analyse for obtaining chemical compositions and morphology information of the synthesized cobalt oxide.

In the second stage, we used the predicted Co(III)/Co(II) ratio from RF1 and corresponding sample mass ratios, scanning rates and synthesis temperatures as inputs. The corresponding capacitances as the output to train a second random forest model RF2. An additional experimental validation was performed to verify the accuracy of the model. Moreover, EIS measurements are utilized to explain the reasons behind capacitance variations.

3.1. Stage1 ML-assisted XPS spectral analysis

3.1.1. Model of RF-assisted XPS

The chemical composition and state of Co-rGO were analysed by X-ray photoelectron spectroscopy (XPS). The Co 2p XPS spectrum of 200-Co-rGO exhibits two characteristic peaks (Co $2p_{3/2}$ 781.1eV and Co $2p_{1/2}$ 796.7eV) and two satellite peaks (785.4eV and 801.7eV), which shown in Fig. 1b [35]. The high intensity of satellite peaks and their shape indicate the existence of Co(II) [36]. Furthermore, the binding energy difference between Co$2p_{3/2}$ and Co $2p_{1/2}$ is close to 16eV, suggesting Co (II) is the sole component when the temperature at 200 °C [37]. The valence states of Co in the experimentally obtained XPS data were analysed (as shown in Fig. 1b-d and SI 1 Fig. S1) and based on the experimental data, RF1 model was established.

The XPS data for the samples 400-Co-rGO (Fig. 1c) clearly shows the two Co states in the spectrum. We observed two new Co(III) characteristic peaks (780.0eV and 794.8eV) and three small new satellite peaks (787.0eV, 797.3eV and 804.0eV). The fitting peaks at 780.0eV and 795.2eV are assigned to Co(III), while the other two peaks at 781.7eV and 797eV are attributed to the presence of Co(II) [35]. Compared with XPS data for 200-Co-rGO samples, Co peak for the 400-Co-rGO sample has red shifted suggesting the formation of Co(III) [35]. Additionally, for the 400-Co-rGO samples, the binding energy difference between Co$2p_{3/2}$ and Co $2p_{1/2}$ is close to 15 eV, which indicates the coexistence of Co(II) and Co(III) [37].

While the XPS peaks of 600-Co-rGO samples exhibited similar characteristic peaks range and shape as of 400-Co-rGO samples. However, the intensity of satellites peaks of 600 °C samples are reduced, suggesting Co(III) is predominant [38].

To quantify the trend of change in chemical composition we introduced a Co(III)/Co(II) ratio aiding in XPS analysis. Supplementary SI 2 Sheet S2 shows the Co(III)/Co(II) at different synthesis temperatures.

Combining the XPS analysis with the machine learning tool, we constructed the RF1 to predict more Co(III)/Co(II) ratios at more extensive experimental conditions. The experimental condition of the XPS samples, which include 8 different mass ratios at 200 °C, 3 different mass ratios at 300 °C, 400 °C, and one mass ratio of 16 wt% at 500 and 600 °C, was combined with corresponding Co(III)/Co(II) ratio to build dataset 1. We emphasise here that experimental conditions act as inputs, and Co(III)/Co(II) ratios act as output (shown in SI 2 Sheet S1). The predicted Co(III)/Co(II) ratio at extensive experimental conditions, including all mass ratios (2 wt% to 16 wt%) and temperature intervals (200–600 °C), are provided in SI 2 Sheet S2.

Fig. 1e exhibits the predicted Co(III)/Co(II) ratio obtained from RF1. Here the X-axis represents the experimental Co(III)/Co(II) ratio, and the Y-axis represents the predicted ratio. The slope of the black line (as typically known in ML-based analysis) is 1 (Fig. 1e) [39]. Here, we can see that the data points are close to the black line, which indicates that predicted and actual values are in good agreement [39] with R-squared value of 0.9997, MAE value of 0.0047 and MSE value of 0.0000618. According to RF1 model, we can say that with the synthesis temperature increasing the Co(III)/Co(II) ratio increases. This demonstrates the potential of utilizing machine learning to predict other XPS results by conducting a small portion of XPS experiments when a large number of XPS measurements are required.

3.1.2. Analysis of chemical compositions and structure

Based on the XPS spectra analysis, it has been confirmed that Co exists in two states: divalent and trivalent. Furthermore, we conducted XRD, Raman, and SEM analysis for samples prepared at (200 °C, 400 °C, and 600 °C) for structural and morphological characteristics and the XPS analysis of Co-rGO materials systems.

Fig. 2a – c shows the O1s spectra in different temperatures, and a noticeable difference can be seen in the range below 532eV. For Fig. 2a, the O_{OH} Peak (531.4eV) of 200-Co-rGO can be assigned to the OH group in $Co(OH)_2$ [35], whereas for 400-Co-rGO (Fig. 2b), the O_{OH} peak disappears, and two new peaks- O_L (529.8eV) and O_V (531.4eV) appear. The O_L corresponds to oxide connected with metal, and O_V is assigned to oxygen defects in the oxide [10]. The observed XPS peaks for 600-Co-rGO and 400-Co-rGO samples locate at a similar position. Thus, it could be understood that $Co(OH)_2$ is retained at low temperatures while transforming into cobalt oxide when temperature increases.

XRD results are shown in Fig. 2 d-e. The XRD analysis was divided into two ranges (18–30°, 35–70°) to avoid high-intensity substrate peaks (~33°). The 200-Co-rGO samples exhibit distinct $Co(OH)_2$ peaks at 19.8°, 38.0°, and 44.0°. Additionally, the minor peak at ~36.3° indicates the presence of a small amount of Co_3O_4. For the synthesis temperature of 400 °C, more peaks of Co_3O_4 (36.3°,43.6°) were observed, while only one $Co(OH)_2$ peak remains at 44°. Furthermore, when the synthesis temperature increases to 600 °C, we can only observe Co_3O_4 peaks in the XRD plots. Thus, it can be concluded that the $Co(OH)_2$, which was initially formed at low temperature, is converted into Co_3O_4 at 600 °C. We observed a weak peak around 28.4° in our XRD plots as shown in Fig. 2d. In order to analyse this peak, we conducted additional XRD measurements of pure GO on carbon fibre paper heated at 200 °C (refer to SI 1, Fig. S2) and observed no peak 28.4°. On analysing further, we noticed that the interplanar spacing (d-value) corresponding to 28.4° closely resembles with d-value of Co_2O_3 (012) plane (refer to "XRD standard reference material card 04-007-3333" and reference [40]). This suggests that the peak at 28.4° might be due to the presence of residual Co_2O_3.

The synthesis and phase transformation processes were also observed in the Raman spectra. The 200-Co-rGO sample exhibited distinct $Co(OH)_2$ peaks at ~460 cm^{-1} and ~640 cm^{-1} [41]. In contrast, the samples 400-Co-rGO mainly displayed characteristic peaks of Co_3O_4 (185 cm^{-1}, 506 cm^{-1}, 690 cm^{-1}) [42]. Specifically, the samples also have a shoulder perk at ~640 cm^{-1} corresponding to the residual $Co(OH)_2$. Furthermore, this residue was barely visible in the 600-Co-rGO samples, which only exhibited characteristic peaks of Co_3O_4. Combining the results of XPS, XRD, and Raman, it could be inferred that the chemical compositions experience a transformation from $Co(OH)_2$ to Co_3O_4 when the synthesis temperature varies from 200 °C to 600 °C. The 200-Co-rGO, 400-rGO-Co and 600-rGO-Co were also characterized by SEM, and the images were shown in SI 1 Fig. S3.

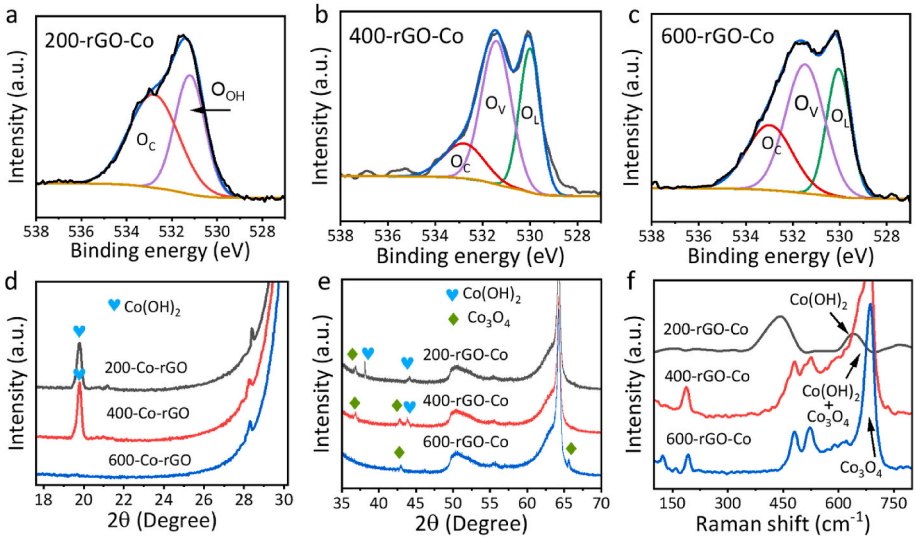

Fig. 2. (a–c) XPS spectrum of O1s of 200 °C, 400 °C, 600 °C samples. XRD pattern of electrode composite heating in different temperatures in the range of (d) 18–30° (e) 33–64° All peak location reference to XRD standard reference material card 00-045-0031 ($Co(OH)_2$) and 01-074-1656(Co_3O_4). (f) Raman spectrum analysis of three different temperatures. (A colour version of this figure can be viewed online.)

3.2. Stage 2 capacitance model establishment and validation

To establish the relationship among synthesis temperatures, Co(III)/Co(II) ratios, and electrochemical properties, we conducted CV experiments and collected data to develop a new RF2 model. These multiple CV scans were conducted in at different synthesis temperature (200–600 °C) and mass ratio (2 wt%-16 wt%). Compared to the experimental conditions of XPS provided above, the experimental conditions for CV have a larger and more comprehensive range. Additionally, we have used different scan rates (100 mV/s - 500 mV/s) to enlarge the dataset and refine the model. All the CV plots are provided in SI 1 Figs. S4–8.

Based on our observations, the variations in the capacitance performance of the samples were similar under different mass ratios or scan rates. Therefore, for convenience, we only present the capacitance trends under 16 wt% and 100 mV/s conditions. (Fig. 3a). For more capacitance results, please refer to the Supplementary Information (SI 1 Figs. S4–S8). With the increase in synthesis temperature, the capacitance first decreases (From Fig. 3a) from 160.9 F/g (for 200-Co-rGO) to 16.0F/g (400-Co-rGO) and then increase to 176.2F/g when the temperature is raised to 600 °C.

Based on CV experiments and RF1, we conclude that temperature variation affects Co(III)/Co(II) ratio and thus influences capacitance. To quantify the correlation, a second random forest model (RF2) was

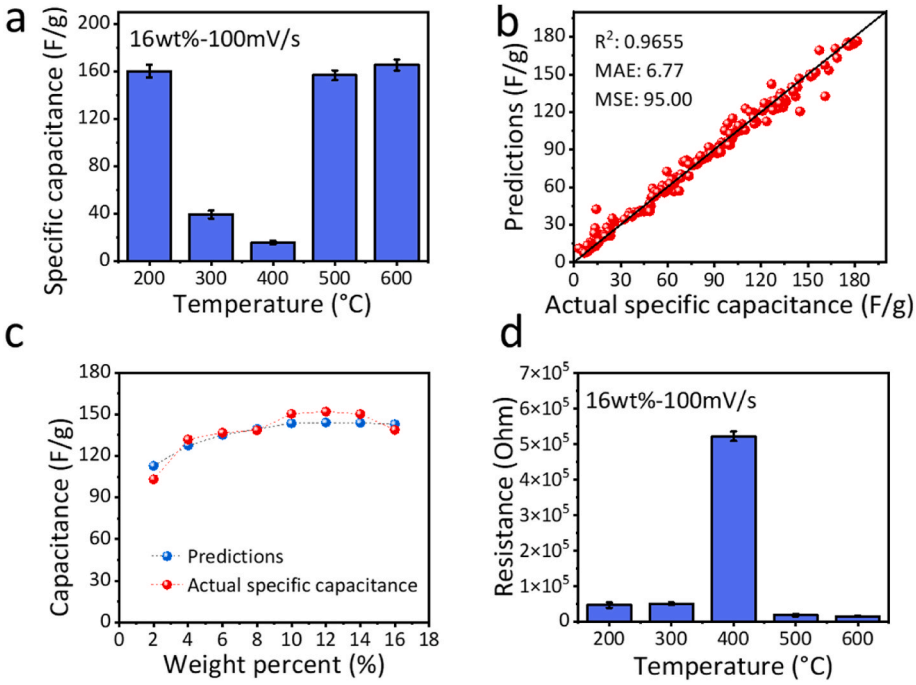

Fig. 3. (a) Capacitance at different temperatures and 16 wt%. (b) Comparison of actual specific capacitance and predicted specific capacitance. (c) Comparison of actual specific capacitance and predicted specific capacitance for experimental validation data (550 °C). (d) Resistance at different temperatures and 16 wt%. (A colour version of this figure can be viewed online.)

constructed. Co(III)/Co(II) ratios from RF1 were combined with Dataset 2 (SI 2 Sheet S3), which include synthesis temperatures (200–600 °C), mass ratios (2 wt%-16 wt%), scan rates (100 mV/s – 500 mV/s), and their corresponding capacitances to establish the Dataset 3 (SI 2 Sheet S4). Thereinto, synthesis temperature, mass ratio, and scan rate act as input, and their corresponding capacitances are output (Fig. 1a Stage 2).

Fig. 3b exhibits the RF2 predicted capacitance, and the black line indicates the best-predicted situation. It can be observed that the data points are distributed centrally along the line. The R-squared value is 0.9655, MAE is 6.77, and the MSE is 95.00. To verify the accuracy of this RF2 model, we compared the experimental validation results at 550 °C with RF2 predicted results (Fig. 3c). It is worth pointing out that predicted values match well with the experimental values with a mean relative error value of less than 8%. As for the relationship between the experimental conditions and capacitance, it can be concluded that the capacitance correlates to the Co(III)/Co(II) ratio, with the least performance for the samples with a ratio proximity of 0.7, and it improves as the ratio deviates from 0.7.

The EIS measurements were performed and presented in Fig. (3d and S9) to understand the reasons for the change in capacitance. The results reveal a highly correlated trend between the diffusion of ions or molecules (Warburg impedance) and the capacitance. It demonstrates that the Warburg slope of 200-Co-rGO and 600-Co-rGO is significantly higher than that of 400-Co-rGO, suggesting the first two samples offer a larger ion transfer rate [43]. This trend could be attributed to the dihydroxylation of $Co(OH)_2$ at 400 °C, resulting formation of a denser mixture of $Co(OH)_2$ and Co_3O_4 [44,45]. The denser oxide increases the resistance at this temperature compared to other temperatures. Thus, it could be inferred that the ion transfer resistance in 200-Co-rGO and 600-Co-rGO is lower than that in 400-Co-rGO, contributing to increased capacitance.

4. Conclusion

We have systematically investigated the effect of temperature on the capacitance of Co-rGO prepared by the hydrothermal method. We used the RF-assisted XPS database to establish a relationship between temperature and Co(III)/Co(II) ratio. The rise of the Co(III)/Co(II) ratio is attributed to an increase in the $Co_3O_4/Co(OH)_2$ ratio with temperature. A machine learning model was developed to predict capacitance under extensive experimental conditions. We also observed that the capacitance is less when the Co ratio approximates 0.7, potentially due to increased ion transfer resistance. The study showcases the efficacy of machine learning, particularly the random forest model, in supporting XPS spectroscopy. This approach offers the dual advantages of reducing resource consumption during extensive XPS measurements and utilizing predicted XPS results for further experimental analysis and computational simulations.

CRediT authorship contribution statement

Xiaoyu Liu: Validation, Investigation, Data curation, Writing – original draft, Visualization. **Dali Ji:** Validation, Investigation, Data curation, Visualization, Validation, Investigation, Data curation, Visualization, Conceptualization, Methodology, Writing – original draft, Writing – review & editing. **Xiaoheng Jin:** Conceptualization, Methodology, Writing – review & editing. **Vanesa Quintano:** Investigation, Writing – review & editing. **Rakesh Joshi:** Investigation, Funding acquisition, Resources, Supervision, Writing – review & editing.

Declaration of competing interest

The authors declare that they have no known competing financial interests or personal relationships that could have appeared to influence the work reported in this paper.

Acknowledgements

Dali Ji acknowledges UNSW Tuition Fee Scholarship and Australian Research Council Discovery Project DP180101436. Vanesa Quintano acknowledges the funding from the European Union's Horizon 2020 research and innovation programme under the Marie Skłodowska Curie Grant Agreement No. 101066462. The authors acknowledge the facilities and the scientific and technical assistance of Microscopy Australia at the Electron Microscope Unit (EMU), Spectroscopy Laboratory and Solid State & Elemental Analysis Unit (SSEAU) within the Mark Wainwright Analytical Centre (MWAC) at UNSW Sydney.

Appendix A. Supplementary data

Supplementary data to this article can be found online at https://doi.org/10.1016/j.carbon.2023.118342.

References

[1] J. Yang, S. Gunasekaran, Electrochemically reduced graphene oxide sheets for use in high performance supercapacitors, Carbon N. Y. 51 (2013) 36–44, https://doi.org/10.1016/j.carbon.2012.08.003.
[2] B. Xu, S. Yue, Z. Sui, X. Zhang, S. Hou, G. Cao, Y. Yang, What is the choice for supercapacitors: graphene or graphene oxide? Energy Environ. Sci. 4 (2011) 2826–2830, https://doi.org/10.1039/c1ee01198g.
[3] M. Segal, Selling graphene by the ton, Nat. Nanotechnol. 4 (2009) 612–614, https://doi.org/10.1038/nnano.2009.279.
[4] J. Lyu, M. Mayyas, O. Salim, H. Zhu, D. Chu, R.K. Joshi, Electrochemical performance of hydrothermally synthesized rGO based electrodes, Mater. Today Energy 13 (2019) 277–284, https://doi.org/10.1016/j.mtener.2019.06.006.
[5] M.F. El-Kady, Y. Shao, R.B. Kaner, Graphene for batteries, supercapacitors and beyond, Nat. Rev. Mater. 1 (2016) 1–14, https://doi.org/10.1038/natrevmats.2016.33.
[6] W. Ma, S. Chen, S. Yang, W. Chen, W. Weng, Y. Cheng, M. Zhu, Flexible all-solid-state asymmetric supercapacitor based on transition metal oxide nanorods/reduced graphene oxide hybrid fibers with high energy density, Carbon N. Y. 113 (2017) 151–158, https://doi.org/10.1016/j.carbon.2016.11.051.
[7] J. Liu, J. Jiang, C. Cheng, H. Li, J. Zhang, H. Gong, H.J. Fan, Co3O4 nanowire@MnO2 ultrathin nanosheet core/shell arrays: a new class of high-performance pseudocapacitive materials, Adv. Mater. 23 (2011) 2076–2081, https://doi.org/10.1002/adma.201100058.
[8] Z. Chen, V. Augustyn, J. Wen, Y. Zhang, M. Shen, B. Dunn, Y. Lu, High-performance supercapacitors based on intertwined CNT/V 2O 5 nanowire nanocomposites, Adv. Mater. 23 (2011) 791–795, https://doi.org/10.1002/adma.201003658.
[9] J. Zhang, J. Jiang, H. Li, X.S. Zhao, A high-performance asymmetric supercapacitor fabricated with graphene-based electrodes, Energy Environ. Sci. 4 (2011) 4009–4015, https://doi.org/10.1039/c1ee01354h.
[10] C. Lai, Y. Sun, B. Lin, Synthesis of sandwich-like porous nanostructure of Co3O4-rGO for flexible all-solid-state high-performance asymmetric supercapacitors, Mater. Today Energy 13 (2019) 342–352, https://doi.org/10.1016/j.mtener.2019.06.008.
[11] E. Lim, J. Changshin, M.S. Kim, M.H. Kim, J. Chun, H. Kim, J. Park, K.C. Roh, K. Kang, S. Yoon, J. Lee, High-performance sodium-ion hybrid supercapacitor based on Nb2O5@Carbon core–shell nanoparticles and reduced graphene oxide nanocomposites, Adv. Funct. Mater. 26 (2016) 3711–3719, https://doi.org/10.1002/adfm.201505548.
[12] Y.Y. Khine, X. Ren, D. Chu, Y. Nishina, T. Foller, R. Joshi, Surface functionalities of graphene oxide with varying flake size, Ind. Eng. Chem. Res. 61 (2022) 6531–6536, https://doi.org/10.1021/acs.iecr.2c00748.
[13] X. Jin, T. Foller, X. Wen, M.B. Ghasemian, F. Wang, M. Zhang, H. Bustamante, V. Sahajwalla, P. Kumar, H. Kim, G.H. Lee, K. Kalantar-Zadeh, R. Joshi, Effective separation of CO2 using metal-incorporated rGO membranes, Adv. Mater. 32 (2020) 1–10, https://doi.org/10.1002/adma.201907580.
[14] D. Ji, Y. Lee, Y. Nishina, K. Kamiya, R. Daiyan, D. Chu, X. Wen, M. Yoshimura, P. Kumar, D.V. Andreeva, K.S. Novoselov, G.H. Lee, R. Joshi, T. Foller, Angstrom-confined electrochemical synthesis of sub-unit-cell non-van der waals 2D metal oxides, Adv. Mater. (2023), 2301506, https://doi.org/10.1002/adma.202301506.
[15] T. Foller, R. Daiyan, X. Jin, J. Leverett, H. Kim, R. Webster, J.E. Yap, X. Wen, A. Rawal, K.K.H. De Silva, M. Yoshimura, H. Bustamante, S.L.Y. Chang, P. Kumar, Y. You, G.H. Lee, R. Amal, R. Joshi, Enhanced graphitic domains of unreduced graphene oxide and the interplay of hydration behaviour and catalytic activity, Mater. Today 50 (2021) 44–54, https://doi.org/10.1016/j.mattod.2021.08.003.
[16] A. Chen, X. Zhang, Z. Zhou, Machine learning: accelerating materials development for energy storage and conversion, InfoMat 2 (2020) 553–576, https://doi.org/10.1002/inf2.12094.
[17] R. Batra, L. Song, R. Ramprasad, Emerging materials intelligence ecosystems propelled by machine learning, Nat. Rev. Mater. 6 (2021) 655–678, https://doi.org/10.1038/s41578-020-00255-y.

[18] P. Simon, Y. Gogotsi, Materials for electrochemical capacitors, Nat. Mater. 7 (2008) 845–854, https://doi.org/10.1038/nmat2297.
[19] B. Selvaratnam, R.T. Koodali, Machine learning in experimental materials chemistry, Catal. Today 371 (2021) 77–84, https://doi.org/10.1016/j.cattod.2020.07.074.
[20] J. Ren, X. Lin, J. Liu, T. Han, Z. Wang, H. Zhang, J. Li, Engineering early prediction of supercapacitors' cycle life using neural networks, Mater. Today Energy 18 (2020), 100537, https://doi.org/10.1016/j.mtener.2020.100537.
[21] N.M. Ralbovsky, I.K. Lednev, Towards development of a novel universal medical diagnostic method: Raman spectroscopy and machine learning, Chem. Soc. Rev. 49 (2020) 7428–7453, https://doi.org/10.1039/d0cs01019g.
[22] Z. Shen, H. Liu, Y. Shen, J. Hu, L. Chen, C. Nan, Machine learning in energy storage materials, Interdiscip. Mater. 1 (2022) 175–195, https://doi.org/10.1002/idm2.12020.
[23] P. Raccuglia, K.C. Elbert, P.D.F. Adler, C. Falk, M.B. Wenny, A. Mollo, M. Zeller, S. A. Friedler, J. Schrier, A.J. Norquist, Machine-learning-assisted materials discovery using failed experiments, Nature 533 (2016) 73–76, https://doi.org/10.1038/nature17439.
[24] N. Sheremetyeva, M. Lamparski, C. Daniels, B. Van Troeye, V. Meunier, Machine-learning models for Raman spectra analysis of twisted bilayer graphene, Carbon N. Y. 169 (2020) 455–464, https://doi.org/10.1016/j.carbon.2020.06.077.
[25] A. Srivastava, O.N. Srivastava, S. Talapatra, R. Vajtai, P.M. Ajayan, Carbon nanotube filters, Nat. Mater. 3 (2004) 610–614, https://doi.org/10.1038/nmat1192.
[26] P. Avouris, M. Freitag, V. Perebeinos, Carbon-nanotube photonics and optoelectronics, Nat. Photonics 2 (2008) 341–350, https://doi.org/10.1038/nphoton.2008.94.
[27] M. Acik, G. Lee, C. Mattevi, M. Chhowalla, K. Cho, Y.J. Chabal, Unusual infrared-absorption mechanism in thermally reduced graphene oxide, Nat. Mater. 9 (2010) 840–845, https://doi.org/10.1038/nmat2858.
[28] B. Zhao, P. Liu, Y. Jiang, D. Pan, H. Tao, J. Song, T. Fang, W. Xu, Supercapacitor performances of thermally reduced graphene oxide, J. Power Sources 198 (2012) 423–427, https://doi.org/10.1016/j.jpowsour.2011.09.074.
[29] L. Rokach, Decision forest: twenty years of research, Inf. Fusion 27 (2016) 111–125, https://doi.org/10.1016/j.inffus.2015.06.005.
[30] Y. Wang, Y. Li, W. Pu, K. Wen, Y.Y. Shugart, M. Xiong, L. Jin, Random bits forest: a strong classifier/regressor for big data, Sci. Rep. 6 (2016) 1–8, https://doi.org/10.1038/srep30086.
[31] B. Prasanth, R. Paul, D. Kaliyaperumal, R. Kannan, Y. Venkata Pavan Kumar, M. Kalyan Chakravarthi, N. Venkatesan, Maximizing regenerative braking energy harnessing in electric vehicles using machine learning techniques, Electron 12 (2023) 1119, https://doi.org/10.3390/electronics12051119.
[32] Z. Wang, Z. Sun, H. Yin, X. Liu, J. Wang, H. Zhao, C.H. Pang, T. Wu, S. Li, Z. Yin, X. F. Yu, Data-driven materials innovation and applications, Adv. Mater. 34 (2022), 2104113, https://doi.org/10.1002/adma.202104113.
[33] F. Tang, D. He, H. Jiang, R. Wang, Z. Li, W. Xue, R. Zhao, The coplanar graphene oxide/graphite heterostructure-based electrodes for electrochemical supercapacitors, Carbon N. Y. 197 (2022) 163–170, https://doi.org/10.1016/j.carbon.2022.06.014.
[34] Y. Sun, Y. Yuan, X. Geng, C. Han, S. Lu, I. Mitrovic, L. Yang, P. Song, C. Zhao, Biochar-derived material decorated by MXene/reduced graphene oxide using one-step hydrothermal treatment as high-performance supercapacitor electrodes, Carbon N. Y. 199 (2022) 224–232, https://doi.org/10.1016/j.carbon.2022.07.058.
[35] P. Gao, Y. Zeng, P. Tang, Z. Wang, J. Yang, A. Hu, J. Liu, Understanding the synergistic effects and structural evolution of Co(OH)2 and Co3O4 toward boosting electrochemical charge storage, Adv. Funct. Mater. 32 (2022), 2108644, https://doi.org/10.1002/adfm.202108644.
[36] Y. Brik, M. Kacimi, M. Ziyad, Y. Brik, F. Bozon-Verduraz, Titania-supported Cobalt and cobalt-phosphorus catalysts: characterization and performances in ethane oxidative dehydrogenation, J. Catal. 202 (2001) 118–128, https://doi.org/10.1006/jcat.2001.3262.
[37] T.J. Chuang, C.R. Brundle, D.W. Rice, Interpretation of the x-ray photoemission spectra of cobalt oxides and cobalt oxide surfaces, Surf. Sci. 59 (1976) 413–429, https://doi.org/10.1016/0039-6028(76)90026-1.
[38] R. Xu, H.C. Zeng, Mechanistic investigation on self-redox decompositions of cobalt-hydroxide-nitrate compounds with different nitrate anion configurations in interlayer space, Chem. Mater. 15 (2003) 2040–2048, https://doi.org/10.1021/cm021732o.
[39] M. Zhou, A. Gallegos, K. Liu, S. Dai, J. Wu, Insights from machine learning of carbon electrodes for electric double layer capacitors, Carbon N. Y. 157 (2020) 147–152, https://doi.org/10.1016/j.carbon.2019.08.090.
[40] J. Chenavas, J.C. Joubert, M. Marezio, Low-spin → high-spin state transition in high pressure cobalt sesquioxide, Solid State Commun. 9 (1971) 1057–1060, https://doi.org/10.1016/0038-1098(71)90462-5.
[41] W.H. Lee, M.H. Han, Y.J. Ko, B.K. Min, K.H. Chae, H.S. Oh, Electrode reconstruction strategy for oxygen evolution reaction: maintaining Fe-CoOOH phase with intermediate-spin state during electrolysis, Nat. Commun. 13 (2022) 605, https://doi.org/10.1038/s41467-022-28260-5.
[42] M. Yu, Z. Wang, C. Hou, Z. Wang, C. Liang, C. Zhao, Y. Tong, X. Lu, S. Yang, Nitrogen-doped Co3O4 mesoporous nanowire arrays as an additive-free air-cathode for flexible solid-state zinc–air batteries, Adv. Mater. 29 (2017), https://doi.org/10.1002/adma.201602868.
[43] C. Alex, S.C. Sarma, S.C. Peter, N.S. John, Competing effect of Co3+Reducibility and oxygen-deficient defects toward high oxygen evolution activity in Co3O4Systems in alkaline medium, ACS Appl. Energy Mater. 3 (2020) 5439–5447, https://doi.org/10.1021/acsaem.0c00297.
[44] R. Salomão, I. Medeiros de Morais Dias, L. Fernandes, Porogenesis in the alumina-brucite-magnesia-spinel system, InterCeram Int. Ceram. Rev. 69 (2020) 46–53, https://doi.org/10.1007/s42411-020-0096-6.
[45] R. Salomão, C.C. Arruda, M.L.P. Antunes, Synthesis, dehydroxylation and sintering of porous Mg(OH)2-MgO clusters, Evolution of Microstructure and Physical Properties (2020), https://doi.org/10.1007/s42411-019-0067-y.